Physics in Medicine & Biology

IPEM
Institute of Physics and
Engineering in Medicine

PAPER

Precision of the PET activity range during irradiation with ^{10}C, ^{11}C, and ^{12}C beams

D Kostyleva[1], S Purushothaman[1,*] ⓘ, P Dendooven[2] ⓘ, E Haettner[1] ⓘ, H Geissel[1,3], I Ozoemelam[4,12],
C Schuy[1], U Weber[1], D Boscolo[1] ⓘ, T Dickel[1,3], V Drozd[1,5], C Graeff[1] ⓘ, B Franczak[1], C Hornung[1], F Horst[1,13],
E Kazantseva[1], N Kuzminchuk-Feuerstein[1], I Mukha[1], C Nociforo[1], S Pietri[1], C A Reidel[1], H Roesch[1,6],
Y K Tanaka[7], H Weick[1], J Zhao[1,8], M Durante[1,9,*] ⓘ, K Parodi[10], C Scheidenberger[1,3,11] and Super-
FRS Experiment Collaboration

1   GSI Helmholtzzentrum für Schwerionenforschung GmbH, Darmstadt, Germany
2   Particle Therapy Research Center (PARTREC), Department of Radiation Oncology, University Medical Center Groningen, University of Groningen, Groningen, The Netherlands
3   II. Physikalisches Institut, Justus-Liebig-Universität, Gießen, Germany
4   Fontys University of Applied Sciences, Eindhoven, The Netherlands
5   Faculty of Science and Engineering, University of Groningen, Groningen, The Netherlands
6   Institute for Nuclear Physics, Technische Universität Darmstadt, Darmstadt, Germany
7   RIKEN Cluster for Pioneering Research, Wako, Japan
8   School of Physics, Beihang University, Beijing, People's Republic of China
9   Department of Condensed Matter Physics, Technische Universität Darmstadt, Darmstadt, Germany
10 Department of Physics, Ludwig-Maximilians Universität München, Munich, Germany
11 Helmholtz Forschungsakademie Hessen für FAIR (HFHF), Campus Gießen, Gießen, Germany
12 Present address: Radiation Oncology, Dana-Farber Cancer Institute and Harvard Medical School, Boston Massachusetts, USA.
13 Present address: OncoRay—National Center for Radiation Research in Oncology, University Hospital Carl Gustav Carus, Technische Universität Dresden, Helmholtz-Zentrum Dresden-Rossendorf, Dresden, Germany.
*   Authors to whom any correspondence should be addressed.

E-mail: s.purushothaman@gsi.de and m.durante@gsi.de

Keywords: particle therapy, radioactive ion beams, carbon ions, PET, range verification

Abstract

Objective. Beams of stable ions have been a well-established tool for radiotherapy for many decades. In the case of ion beam therapy with stable ^{12}C ions, the positron emitters ^{10,11}C are produced via projectile and target fragmentation, and their decays enable visualization of the beam via positron emission tomography (PET). However, the PET activity peak matches the Bragg peak only roughly and PET counting statistics is low. These issues can be mitigated by using a short-lived positron emitter as a therapeutic beam. *Approach.* An experiment studying the precision of the measurement of ranges of positron-emitting carbon isotopes by means of PET has been performed at the FRS fragment-separator facility of GSI Helmholtzzentrum für Schwerionenforschung GmbH, Germany. The PET scanner used in the experiment is a dual-panel version of a Siemens Biograph mCT PET scanner. *Main results.* High-quality in-beam PET images and activity distributions have been measured from the in-flight produced positron emitting isotopes ^{11}C and ^{10}C implanted into homogeneous PMMA phantoms. Taking advantage of the high statistics obtained in this experiment, we investigated the time evolution of the uncertainty of the range determined by means of PET during the course of irradiation, and show that the uncertainty improves with the inverse square root of the number of PET counts. The uncertainty is thus fully determined by the PET counting statistics. During the delivery of 1.6×10^7 ions in 4 spills for a total duration of 19.2 s, the PET activity range uncertainty for ^{10}C, ^{11}C and ^{12}C is 0.04 mm, 0.7 mm and 1.3 mm, respectively. The gain in precision related to the PET counting statistics is thus much larger when going from ^{11}C to ^{10}C than when going from ^{12}C to ^{11}C. The much better precision for ^{10}C is due to its much shorter half-life, which, contrary to the case of ^{11}C, also enables to include the in-spill data in the image formation. *Significance.* Our results can be used to estimate the contribution from PET counting statistics to the precision of range determination in a particular carbon

therapy situation, taking into account the irradiation scenario, the required dose and the PET scanner characteristics.

1. Introduction

With the first clinical trial using proton beams in 1954, the Lawrence Berkeley Laboratory and the University of California Berkeley pioneered the field of ion-beam therapy (Tobias *et al* 1958). During the next four decades, the laboratory extensively investigated the use of heavier ions up to argon (Castro *et al* 1980) as well as the use of radioactive beams and performed the first in-beam positron emission tomography (PET) imaging (Llacer *et al* 1979). Considering the relatively low linear energy transfer (LET) in the entrance channel and the favourable peak-to-plateau ratio, carbon ions were then selected to be used first in Japan and then in Europe (Durante *et al* 2021).

Compared to electrons and photons, ion beams provide superior depth-dose characteristics because they deposit the highest dose at the end of their atomic range, in the so-called Bragg peak. This property makes them, in general, better suited for treating localized deep-seated tumor volumes because the integral dose delivered to healthy tissue and organs at risk is lower, resulting in less side effects and a better quality of life for patients. In order to avoid depositing a high dose in normal tissue/organs at risk that are located next to the tumor to be irradiated and at the same time guarantee the tumor coverage, the location of the Bragg peak needs to be accurately known. In practice, uncertainties in the Bragg peak location during patient irradiation originate from anatomical changes in the patient during the course of the treatment, patient setup errors and inherent uncertainties in the conversion of the planning computed tomography image to particle stopping power ratio relative to water (Knopf and Lomax 2013). These uncertainties are presently taken into account via safety margins in robust treatment planning and contribute to the proper selection of beam angles which avoid stopping the beam in front of organs at risk (Unkelbach *et al* 2007, Pflugfelder *et al* 2008, Liu *et al* 2012, Wolf *et al* 2020). These factors lead to safe but, unavoidably, not optimal treatment plans.

Among the efforts aimed at reducing the range uncertainty, techniques for *in vivo* range verification have been and are being developed and implemented. As the ion beam stops in the patient, such techniques make use of secondary radiation created via the interaction of the beam with the patient (Smeets *et al* 2012). One of the most advanced techniques employs PET imaging of the positron-emitting radioactive nuclei in therapy with stable ion beams, where radioactive nuclei are created in nuclear reactions of the primary ions and the atomic nuclei in the patient. Positron emitters are produced by nuclear fragmentation reactions of both the primary beam ions and the atomic nuclei in the patient, respectively called projectile and target fragmentation. PET of these positron emitters for a range verification technique was first proposed by Maccabee *et al* in 1969 (Maccabee *et al* 1969). Since then, it has become one of the most used range-verification tools in ion beam therapy (Pawelke *et al* 1997, Parodi *et al* 2002, Enghardt *et al* 2004, Fiedler *et al* 2010, 2012, Parodi 2015). In the case of ion beam therapy with ^{12}C ions, the most relevant positron emitters are ^{11}C and ^{10}C produced in projectile fragmentation. The characteristics of these isotopes are shown in table 1. PET imaging of these positron emitters for range verification has two disadvantages: the peak of the PET activity created by stable beams is only somewhat proximal to the Bragg peak (Fiedler *et al* 2012) and the activity of positron emitters created is small, due to the relatively low probability of nuclear reactions to happen. The latter, in combination with the comparably long half-life of ^{11}C, necessitates relatively long measurement times, leaving time for metabolic wash-out of the positron emitters (Kraan 2015, Toramatsu *et al* 2018).

A way forward is to use a beam of short-lived positron-emitters for therapy: the position of their PET activity peak is very close to the Bragg peak and the positron emission activity is much larger, allowing shorter PET measurement times. In the pioneering work at Lawrence Berkeley National Laboratory in the early 1980s, the technique was first used as a low-dose probe beam for pre-treatment localization of malignant tissue prior to the heavy-ion therapy with stable beams (Chatterjee *et al* 1981, 1982, Llacer *et al* 1984). Ever since the closure of the ion beam therapy program at Berkeley in 1992, HIMAC, Japan, has been the front-runner in the field of hadron therapy with radioactive beams, focusing on the positron-emitting isotopes of carbon and oxygen (Kanazawa *et al* 2002, Iseki *et al* 2004, Mohammadi *et al* 2019, Chacon *et al* 2020). At the early stage of ion beam therapy investigations at GSI, the in-beam PET imaging using radioactive ion beams was investigated (Enghardt *et al* 1992). A comprehensive review of the topic can be found in (Durante and Parodi 2020).

A new initiative on the Biomedical Applications of Radioactive ion Beams (BARB; www.gsi.de/BARB) started at GSI in 2020, aiming at, amongst others, pre-clinical validation of *in vivo* beam visualization in heavy ion beam therapy with positron emitting carbon and oxygen isotopes and basic studies in this context (Boscolo *et al* 2021). The present work is one of the first contributions to this initiative. It is devoted to the following. Beams of the positron-emitting nuclides ^{11}C and ^{10}C were produced and separated in-flight at the fragment separator FRS
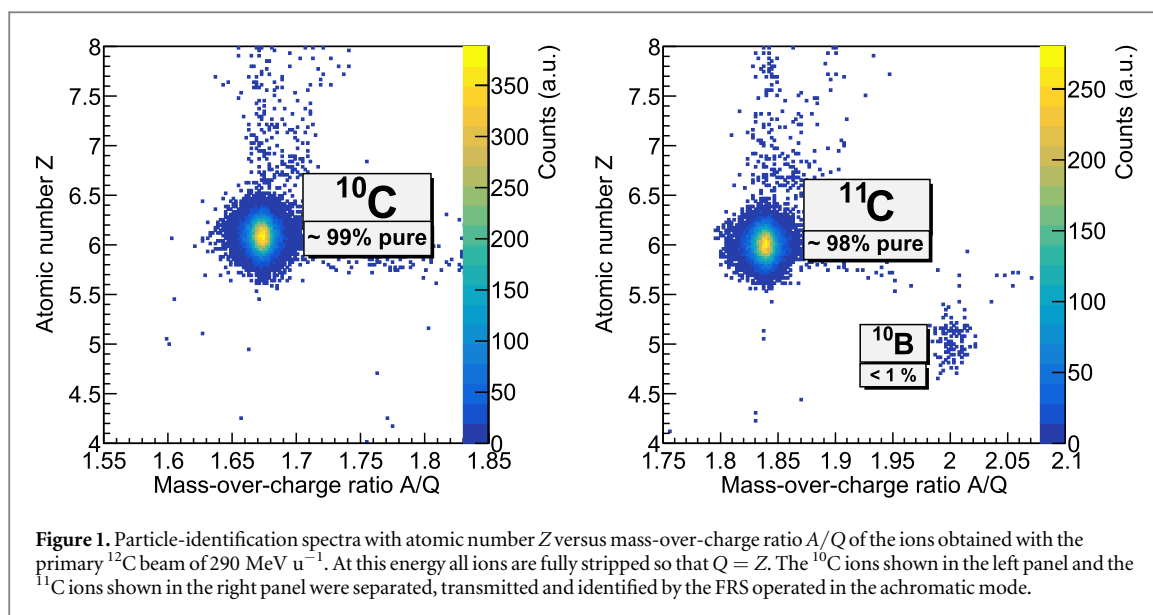
Figure 1. Particle-identification spectra with atomic number Z versus mass-over-charge ratio A/Q of the ions obtained with the primary ^{12}C beam of 290 MeV u^{-1}. At this energy all ions are fully stripped so that $Q = Z$. The ^{10}C ions shown in the left panel and the ^{11}C ions shown in the right panel were separated, transmitted and identified by the FRS operated in the achromatic mode.

Table 1. The characteristics of $^{10, 11}$C isotopes relevant for this study.

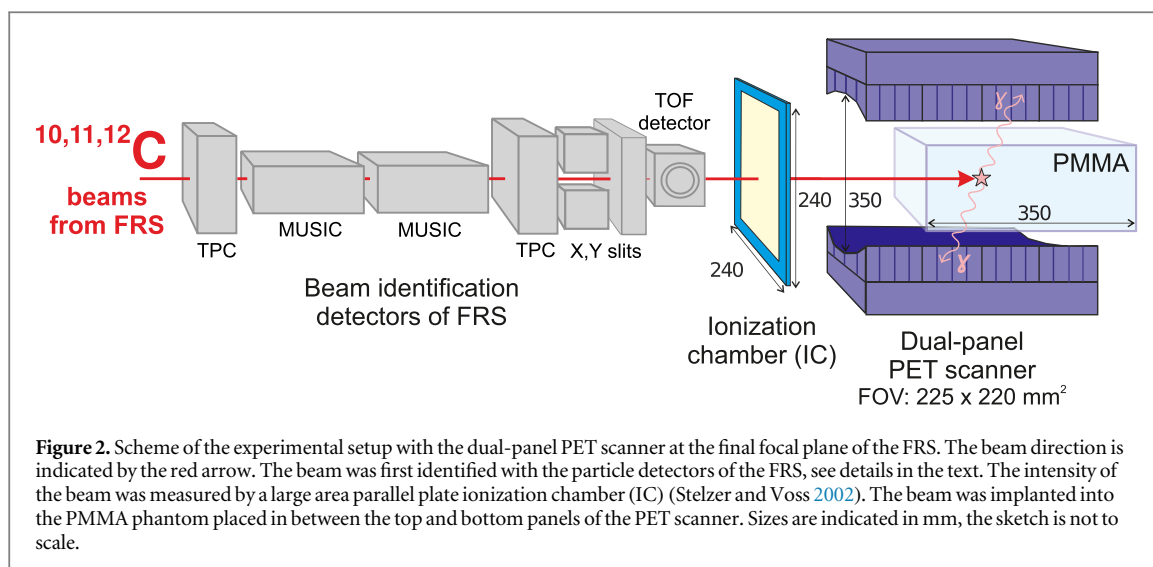| Isotope	Half-life	Prompt gamma-ray emission	Positron-emission end-point energy	RMS effective positron range in water
^{11}C	20.4 min	—	0.96 MeV	0.4 mm
^{10}C	19.3 s	718 keV at 100% branching ratio	1.90 MeV	1.2 mm

of GSI(Geissel *et al* 1989, 1992) with the aim to investigate the relationship between the precision in range determination obtained from the PET image and the number of positron-emitting isotopes injected. For comparison and for reference, beams of stable ^{12}C ions were also used. The beams were implanted in PMMA (polymethyl methacrylate, $(C_5O_2H_8)_n$, density of 1.18 g cm^{-3}) phantoms and in-beam positron emission imaging was performed using a dual-panel scanner. Activity distributions obtained from the images were analyzed from the point of view of statistics. The results of the presented analysis can be used as a starting point to predict the achievable precision of range in realistic patient treatment scenarios depending on the collected PET statistics.

2. Materials and methods

2.1. Radioactive ion beams produced with the fragment separator FRS

The radioactive beams of interest, ^{10}C and ^{11}C, were produced with the in-flight fragment separator and magnetic spectrometer FRS (Geissel *et al* 1992) of GSI. Stable beams of ^{12}C with energies of 380 MeV u^{-1} and 290 MeV u^{-1} and intensities up to 10^9 ions s^{-1} were delivered to the entrance of the FRS by the combination of the linear accelerator UNILAC (Angert and Schmelzer 1969) and the synchrotron SIS18 (Steiner *et al* 1992). Beams of the positron emitters ^{10}C and ^{11}C were produced via nuclear fragmentation of the ^{12}C ions in an 8 g cm^{-2} thick beryllium target. Downstream of the target, radioactive beams were separated in-flight using the twice magnetic rigidity analysis and energy loss in a shaped degrader ($B\rho$-ΔE-$B\rho$) technique (Geissel *et al* 1992) and delivered to the final focal plane of the FRS, where the phantom and PET scanner setup was located. The in-flight particle identification was performed with the $B\rho$-ΔE-TOF method (Geissel *et al* 1992) using the standard particle detectors of FRS: TPC tracking detectors (Janik *et al* 2011), MUSIC energy-loss detectors (Stolz *et al* 2002) and TOF time-of-flight detectors, see e.g. (Kurcewicz *et al* 2012). Examples of identified secondary ^{10}C and ^{11}C beams are shown in figure 1. The level of contaminants in this experiment was on the order of few percent (Boscolo *et al* 2022).

The FRS was operated in its standard ion-optical mode, characterized by being overall achromatic with an acceptance of 20 π mm mrad and a momentum spread $\Delta p/p$ of 2% (FWHM). A wedge degrader was used for spatial separation. The angle of the degrader was chosen either such that the overall achromatism was preserved or to achieve momentum compression (mono-energetic mode) in order to minimize the range straggling. The mono-energetic mode is characterized by a reduced momentum spread but a larger size of the beam spot in the lateral direction in the focal plane, see e.g. the image of ^{11}C in figure 6(b). The mono-energetic mode is often

Figure 2. Scheme of the experimental setup with the dual-panel PET scanner at the final focal plane of the FRS. The beam direction is indicated by the red arrow. The beam was first identified with the particle detectors of the FRS, see details in the text. The intensity of the beam was measured by a large area parallel plate ionization chamber (IC) (Stelzer and Voss 2002). The beam was implanted into the PMMA phantom placed in between the top and bottom panels of the PET scanner. Sizes are indicated in mm, the sketch is not to scale.

used in implantation experiments in order to minimize the range spread in the stopper material (Geissel *et al* 1989, Weick *et al* 2000, Scheidenberger *et al* 2003). In this experiment, the measured momentum spread $\Delta p/p$ was about 0.8% (FWHM).

In the achromatic mode, the beam is focused on the same spot at the final focus regardless of the initial angular or momentum deviation. An achromatic beam is relevant for radiotherapy using carbon ions. Therefore, in this paper, mainly the results of the image analysis of the achromatic ^{10,11}C beams are presented. The $\Delta p/p$ of the ion beam for the achromatic measurements varied within 1.2%–1.8% (FWHM). This is a realistic approximation for carbon ion therapy beams behind a ripple filter.

2.2. PET setup

2.2.1. Dual-panel PET scanner

The positron emitters ^{10,11}C produced and separated by the FRS and the stable primary beam ^{12}C were implanted into blocks of PMMA (phantom, see section 2.2.2 for details), and their high-quality planar PET images were obtained using a modified version of a Siemens Biograph mCT PET scanner. The scheme of the setup with the PET scanner at the final focal plane of the FRS is shown in figure 2. The scanner was previously used at the PARTREC facility in Groningen, the Netherlands, to study real-time PET imaging of proton and helium beams (Ozoemelam *et al* 2020a, 2020b). This scanner is essentially 1/6 of a Siemens Biograph mCT clinical scanner (Jakoby *et al* 2011). The scanner panels were mounted above and below the implantation phantom. The panels are curved in the direction perpendicular to the beam line with a radius of curvature of 42.1 cm and flat in the direction along the beam line. The distance between the centers of the front faces of the panels was 35 cm, providing an angular coverage of 130 degrees. This resulted in a coincidence detection efficiency of 1.4% measured with a ^{22}Na point source placed in the middle of the field of view (FoV), including attenuation in the PMMA phantom covering the full FoV. Each scanner panel is made out of a 4×4 array of block detectors, resulting in a FoV of 225×220 mm^2. The FoV is slightly smaller in one direction due to the curvature of the panel. Each block detector consists of a 13×13 array of $4 \times 4 \times 20$ mm^3 LSO (lutetium oxyorthosilicate doped with cerium) scintillation crystals read out by a 2×2 array of PhotoMultiplier Tubes (PMTs).

Coincidences between any pair of detectors from the opposing panels that detect a 511 keV positron annihilation photon are recorded in event list mode for further processing. Each event contains the identification of the two scintillation crystals involved and the time difference between the detection by the two crystals (the so-called time-of-flight, ToF, information). An energy window of 435–650 keV and a coincidence time window of 4.1 ns were used. The influence of a prompt 718 keV gamma ray from ^{10}C decay on the image quality is considered to be negligible. This is based on the comparison between the measurements with two sources: a pure positron emitter ^{68}Ge and a ^{22}Na positron emitter which gives an additional 1275 keV prompt gamma ray. The coincidence resolving time of the scanner is 550 ps FWHM, enabling the localization of a positron annihilation event along the line of response (LOR) with a spatial resolution of 8 cm FWHM. As the vertical extent of the stopping distribution of the beams used in our work is quite a bit smaller than this value, the ToF information is not used in the image. The spatial resolution of the scanner in the center of the FoV is around 4 mm (FWHM) (Jakoby *et al* 2011). The value of 5.5 mm (FWHM) was measured during this experiment with the ^{22}Na point source placed in the middle of scanner's FOV. A timestamp is introduced in the event file every millisecond, enabling to generate time-dependent results with a resolution of 1 ms. The fraction of random coincident events is

determined by recording coincidences in a delayed time window during each data acquisition. Such delayed coincident events are marked in the list mode files and removed during data analysis.

2.2.2. PMMA phantom

The implantation phantom was a homogeneous PMMA block with a size of $120 \times 250 \times 350$ mm^3. The phantom was placed in-between the two PET scanner panels with its long side in the beam direction and its short side in the vertical direction, see figure 2. The PMMA phantom was placed at different positions relative to the scanner's FoV, each position chosen such that the ions stopped in the center of the FoV, where the scanner sensitivity is highest. PMMA positions were chosen based on the estimates of the energy at the entrance of the phantom and thus the range in the phantom using the LISE++ simulation package (Tarasov and Bazin 2008) prior to the experiment. In the coordinate system of the scanner (centered in the center of the FoV), the positions of the front face of the PMMA along the beam direction x were -103 mm and -39 mm corresponding to the primary beam energies of 380 MeVu^{-1} and 290 MeV u^{-1}, respectively. The experiment with the higher-energy ^{12}C beam was performed during a separate experiment using a primary beam of ^{16}O at 370 MeV u^{-1} and with a PMMA position of -70 mm. In this case, the ^{12}C ions were implanted about 3 cm past the center of the FoV. After each measurement, the phantom was exchanged in order to avoid the influence of activation.

The activity measurements were immediately followed by a measurement of the depth-dose distribution of the same beam by a high-precision water column setup placed downstream of the PET scanner (not shown in figure 2). This provided independent range measurements of the incoming beams, see (Boscolo *et al* 2022) for details.

2.2.3. Beam intensity measurement

A dedicated gas-filled ionization chamber (IC) capable of measuring high rates (Stelzer and Voss 2002) was placed upstream of the implantation phantom to record the beam intensity during the high-intensity imaging runs, see figure 2. Prior to the imaging measurements, the IC was calibrated with a low-intensity primary beam of ^{12}C using the counting rate of a BC-400 scintillation detector. The latter detector belongs to the beam identification detectors of the FRS. The ^{10,11,12}C beams implanted into PMMA phantom had intensities of 10^6 to 10^7 ions/spill, respectively. The intensity of the implanted ^{10}C beam was on average about an order of magnitude lower than that of the ^{11}C beam. This can be explained by an order of magnitude difference between the production cross-sections of these isotopes from the ^{12}C beam (Horst *et al* 2019).

2.3. Analysis

2.3.1. Image reconstruction

The images of the implanted isotopes of carbon were reconstructed following the procedure described in (Ozoemelam *et al* 2020a). The identifications of the opposite crystals in each coincidence event were converted into the coordinates in space considering the curved geometry of the scanner. The block detector does not provide information on where the interaction of a gamma ray inside the crystal happened. Thus, the interaction point was determined by a randomly-chosen location across the 4×4 mm^2 crystal's cross-section and a randomly-chosen depth-of-interaction (DOI) along the 20 mm length of the crystal. The random sampling of the DOI was performed according to an exponential decay curve representing the attenuation of 511 keV gamma rays in LSO. The two interaction points thus determined are the end points of the LOR for the event. The images were created as the two-dimensional histogram of the crossing points of the LORs with the middle plane between the two scanner heads (this plane being the central plane of the beam). Reconstruction was performed with a 2×2 mm^2 pixel size.

2.3.2. Sensitivity and attenuation correction

Quantitative 2D images can only be obtained after introducing corrections for the attenuation of gamma rays in the phantom and the scanner's sensitivity. The latter has its maximum in the center of the FoV and drops almost linearly towards its edges (Ozoemelam *et al* 2020a). These two correction parameters were simultaneously measured as follows. A 10 mm high and 210 mm wide opening along the full length of a PMMA phantom was cut out. A ^{22}Na point source could thus be placed in the image plane 'inside' the phantom. The ^{22}Na source used has an active volume of 1 mm diameter and an activity of 1.438 MBq. It is encapsulated in a 4 mm thick plastic disk of 25.4 mm diameter. The position of the ^{22}Na point source was varied across the image plane on a regular 2D grid with 10 mm spacing. For each source position, 10^6 coincidence events were recorded. The measurement procedure was repeated for each PMMA phantom position that was used during the experiment with the beam. The background rate (in the absence of the source) was measured for 300 s for each PMMA position. The resulting set of point-source measurements for each PMMA position was used to construct the 2D sensitivity and

attenuation correction map. The difference in attenuation between the cut-out phantom used for this calibration and the solid phantom used during the beam experiment can be neglected here.

Prior to the image reconstruction of the source data, the number of events accumulated at each source position was corrected by the number of random coincidence events. The ratio of random to true coincidences for the positions of the ^{22}Na source varied from 0.5 to 3.5%. The ratio is the lowest for the source position in the center of the FoV, and increases when the source is moved towards the FoV's periphery. The background measurements exhibited a random to true ratio close to 100%.

After the correction for random events, the image of the source data was reconstructed as described in section 2.3.1. The x and y coordinates of the source position were determined as the mean values of fits with a Gaussian function for the projection of the peak on the x and y directions. This procedure is more consistent than relying on the values given by the source positioning system, which had an accuracy of about 2 mm.

The rate of the true events R for each source position was calculated as

$$R = N/t - R_{bg}, \tag{1}$$

where N is the total number of coincidence events corrected for random events, t is the data acquisition time and R_{bg} is the background rate corrected for random events. The sensitivity and attenuation correction factor S was then obtained as

$$S = R/(A \cdot br), \tag{2}$$

where A is the activity of the ^{22}Na point source and br the branching ratio for positron emission of 0.9030(9) taken from the literature (Bé *et al* 2010). Having determined S for the positions of the source on a 10 mm step grid, the points in-between were linearly interpolated. As a result, the 2D sensitivity and attenuation correction map was constructed, see section 3.1.

2.3.3. ^{10,11}C activity profiles

The 2D PET images, reconstructed as described in section 2.3.1, were divided by the corresponding sensitivity and attenuation correction map. The 1D activity distributions in the direction of the beam were derived by summing the reconstructed PET images over a 40 mm wide region perpendicular to the beam direction. This width corresponds to about 2σ and 1σ of the lateral width of the achromatic and mono-energetic beams, respectively. This information is derived from the position distributions of the beams as measured by the identification detectors of the FRS (Kurcewicz *et al* 2012) and extrapolated to the position of the PMMA entrance.
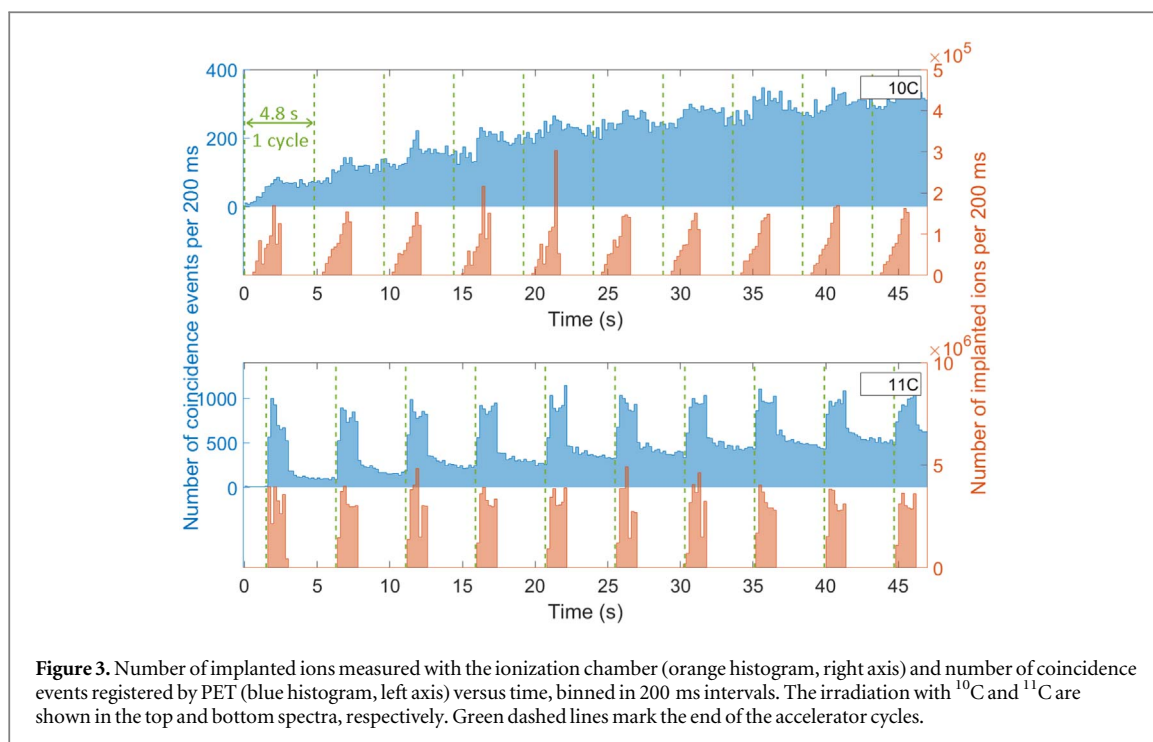
2.3.4. Time structure of the implanted beams

The beam implanted into PMMA had a pulsed structure: a spill length of 2.0 s was followed by a beam-off period of 2.8 s (the full cycle is thus 4.8 s). This incoming particle time structure was stable to 0.1 s. Such a spill structure was typically used during carbon ion therapy at GSI (Enghardt *et al* 1999). In addition to the intensity measurement by the IC, see section 2.2.3, the time structure of the beam is also visible in the PET data. The time evolution of the intensity of the ^{10}C and ^{11}C beams as derived from the IC data and the number of coincidence events from the PET data are shown in figure 3. The IC and PET time histograms are synchronized by the start of the first spill, and are shown overlapped for illustration purposes.

During the spills, more coincidence events are registered by the PET scanner than during the beam-off periods. These events can be related to the fast-decaying positron-emitters with half-lives in the millisecond range and with high positron endpoint energies as well as to prompt γ-emission from excited nuclear levels. These in-spill events might broaden the spatial distribution of the positron-emitters of interest and are usually excluded from the data analysis, see e.g. (Pawelke *et al* 1997, Parodi *et al* 2002). One can most clearly see the spikes from prompt events in every spill in the case of the ^{11}C irradiation. Therefore, for ^{11}C the in-spill events were excluded from the data analysis, and only the events belonging to beam-off periods were used for image reconstruction. The same selection was applied to the ^{12}C data. However, no major prompt component relative to the PET counts is visible in the ^{10}C case. We verified that the analysis of the full data gives the same activity peak precision versus PET counts as the analysis of the beam-off data only. For ^{10}C, we thus use all the registered events as this maximizes the coincidence rate. The difference between ^{10}C and ^{11}C is due to the difference in half-life: ^{10}C decays 64 times faster than ^{11}C and thus the prompt component is relatively lower by the same factor (assuming the prompt component normalized to the beam intensity is the same for ^{10}C and ^{11}C).

2.3.5. Fitting of the PET activity profiles

To describe the characteristic shape of the PET activity distribution at the region of interest, i.e. the activity peak, it is necessary to consider an asymmetric peak shape. In this case, a central Gaussian smoothly connected with exponential functions at both or one of the peak edges represents the experimental data better than a pure Gaussian (Routti and Prussin 1969). The assumption here is that these functions and their first derivatives are

Figure 3. Number of implanted ions measured with the ionization chamber (orange histogram, right axis) and number of coincidence events registered by PET (blue histogram, left axis) versus time, binned in 200 ms intervals. The irradiation with ^{10}C and ^{11}C are shown in the top and bottom spectra, respectively. Green dashed lines mark the end of the accelerator cycles.

continuous at the joining point. This Gaussian-exponential function will be represented by its acronym GE in the following. The GE function used in the further-described analysis has five parameters, namely, the mean and the standard deviation of the central Gaussian, distances to the points where the exponents on the trailing and the leading edge start and a constant background. The maximum of the GE peak coincides with the mean of the central Gaussian and the range of PET activity is defined by this parameter. It will be referred to as peak position in the following. The data were fitted with the GE function using the curve-fitting routine of the commercial software program Igor Pro. The reduced chi-square (χ^2_{red}) test for goodness-of-fit is used as a criterion for selecting the fit region.

The GE function was able to represent the height of the activity peak from under 20% up to the maximum at both proximal and distal fall-off regions of the ^{10}C and ^{11}C data sets. In the case of ^{12}C, the fit region covers 50% to the maximum at the proximal edge and 60% to the maximum of the distal fall-off region. Typical examples of the fit results from both low and high statistics cases are shown in figure 4. It presents also the comparison between Gaussian and GE fits to the data in terms of goodness-of-fit.
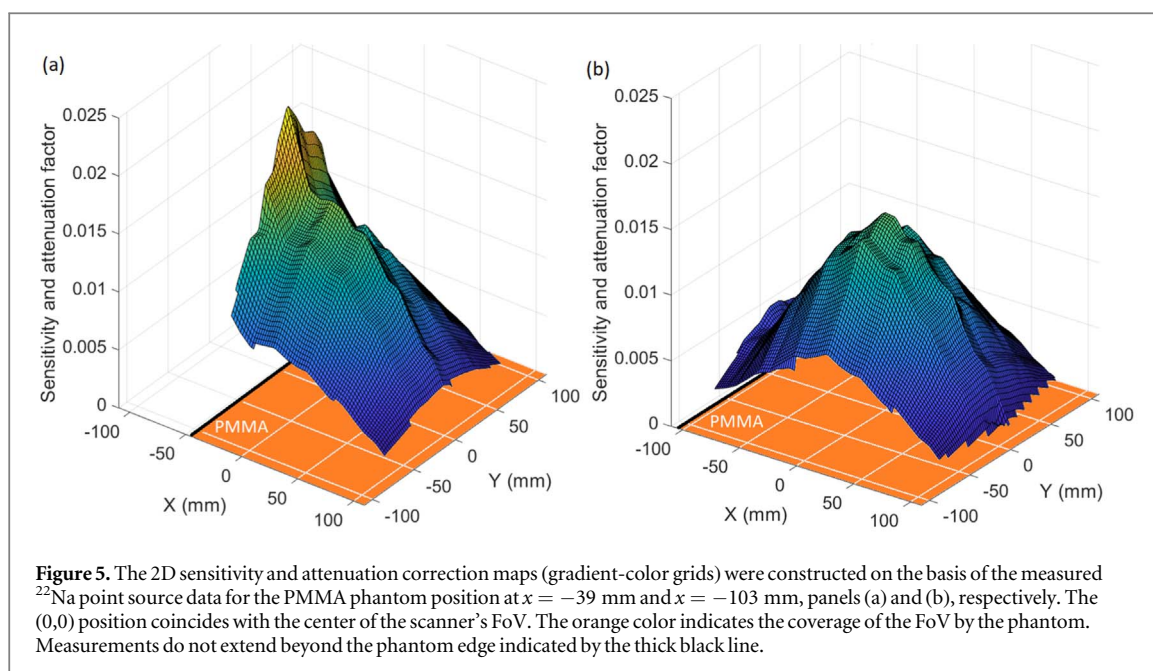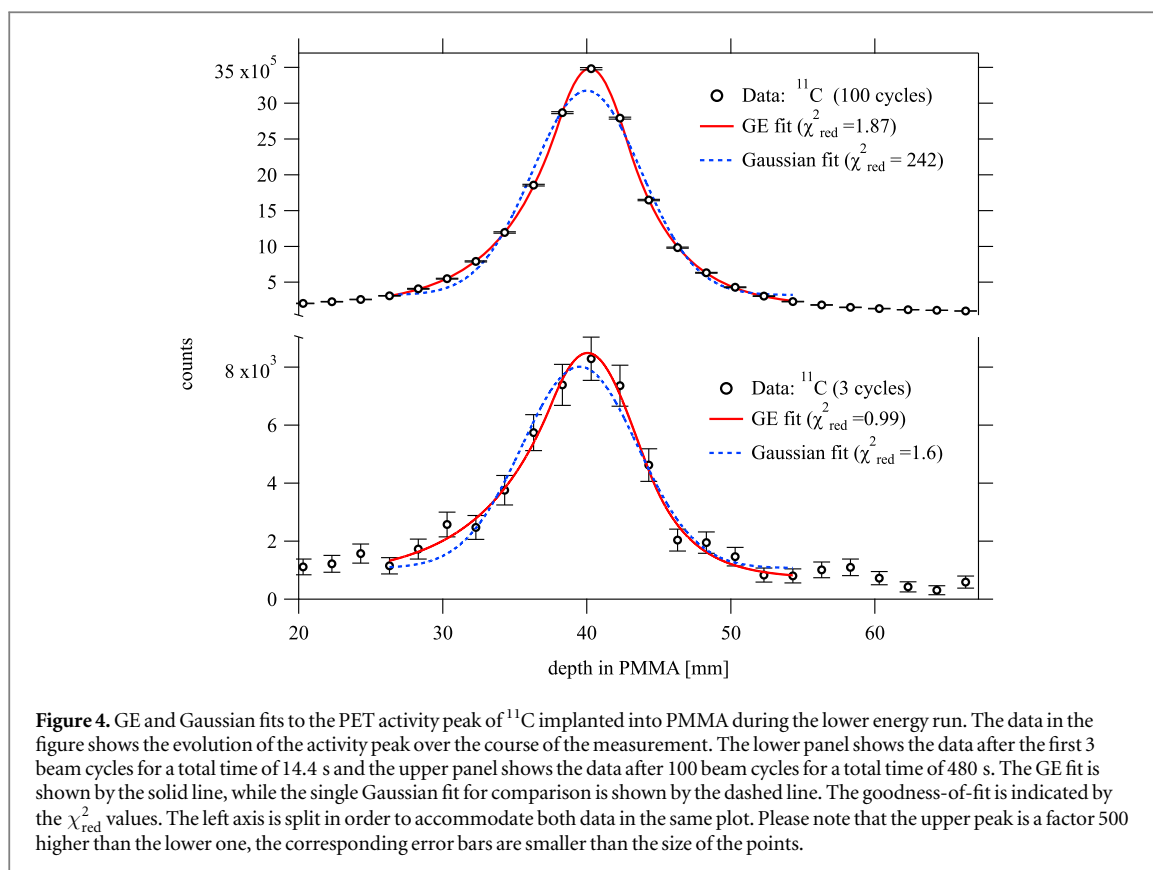
3. Results

3.1. Sensitivity and attenuation correction maps
The sensitivity and attenuation correction maps built for the phantom positions at $x = -39$ mm and $x = -103$ mm are shown in figure 5, panels (a) and (b), respectively. The maps capture the sensitivity fluctuations arising from the peculiarities in the scanner's construction, e.g. the gaps of about 4 mm between the scintillator crystal arrays of neighbouring block detectors, and geometric effects due to the coincidence nature of the recorded events. The map in panel (a) built for the PMMA position of $x = -39$ mm exhibits a rise of the sensitivity towards the phantom's edge, due to the decrease in attenuation when approaching the edge. The situation is different, see panel (b), when the PMMA edge is at $x = -103$ mm so that it covers almost the full FoV. In general, the attenuation in the latter case is higher due to the fact that the annihilation photons have to pass through more phantom material before reaching the scanner panels. This is reflected in the maps.

3.2. PET images and activity profiles of ^{10,11,12}C
The corrected images of ^{10,11,12}C ions implanted into the PMMA phantom during the higher energy run and the lower energy run are shown in figure 6 in panels (a) and (b), respectively. Measurement with the water column confirms that the different beams of each panel (a) and (b) have the same range in water within 1 mm, see table 2. The image of the ^{11}C beam in figure 6(b) exhibits a larger lateral spread compared to the other images because this measurement was taken in the mono-energetic mode of the FRS operation, see section 2.1 for details. The

Figure 4. GE and Gaussian fits to the PET activity peak of ^{11}C implanted into PMMA during the lower energy run. The data in the figure shows the evolution of the activity peak over the course of the measurement. The lower panel shows the data after the first 3 beam cycles for a total time of 14.4 s and the upper panel shows the data after 100 beam cycles for a total time of 480 s. The GE fit is shown by the solid line, while the single Gaussian fit for comparison is shown by the dashed line. The goodness-of-fit is indicated by the χ^2_{red} values. The left axis is split in order to accommodate both data in the same plot. Please note that the upper peak is a factor 500 higher than the lower one, the corresponding error bars are smaller than the size of the points.

Figure 5. The 2D sensitivity and attenuation correction maps (gradient-color grids) were constructed on the basis of the measured ^{22}Na point source data for the PMMA phantom position at $x = -39$ mm and $x = -103$ mm, panels (a) and (b), respectively. The (0,0) position coincides with the center of the scanner's FoV. The orange color indicates the coverage of the FoV by the phantom. Measurements do not extend beyond the phantom edge indicated by the thick black line.

other images were taken in the achromatic mode. The image of ^{12}C in figure 6(a) was obtained during a separate experiment, see section 2.2.2 for details.

The 1D PET activity profiles, obtained from the corresponding images, are shown in figure 7. One observes a difference in the location of the activity peaks produced by the ^{12}C and ^{10,11}C nuclei. This can be explained by the difference in the origin of positron emitters. The activity distribution induced by ^{12}C is obtained indirectly, via imaging of the positron-emitters formed via fragmentation of the ^{12}C projectiles and target nuclei. The latter creates an activity plateau (target fragmentation) superimposed on the activity peak from projectile fragmentation which is mainly contributed by the ^{11}C and ^{10}C ions. This peak shows a distal tail because some of the projectile fragments with lower atomic numbers have a longer range than the primary ^{12}C beam. In the case of
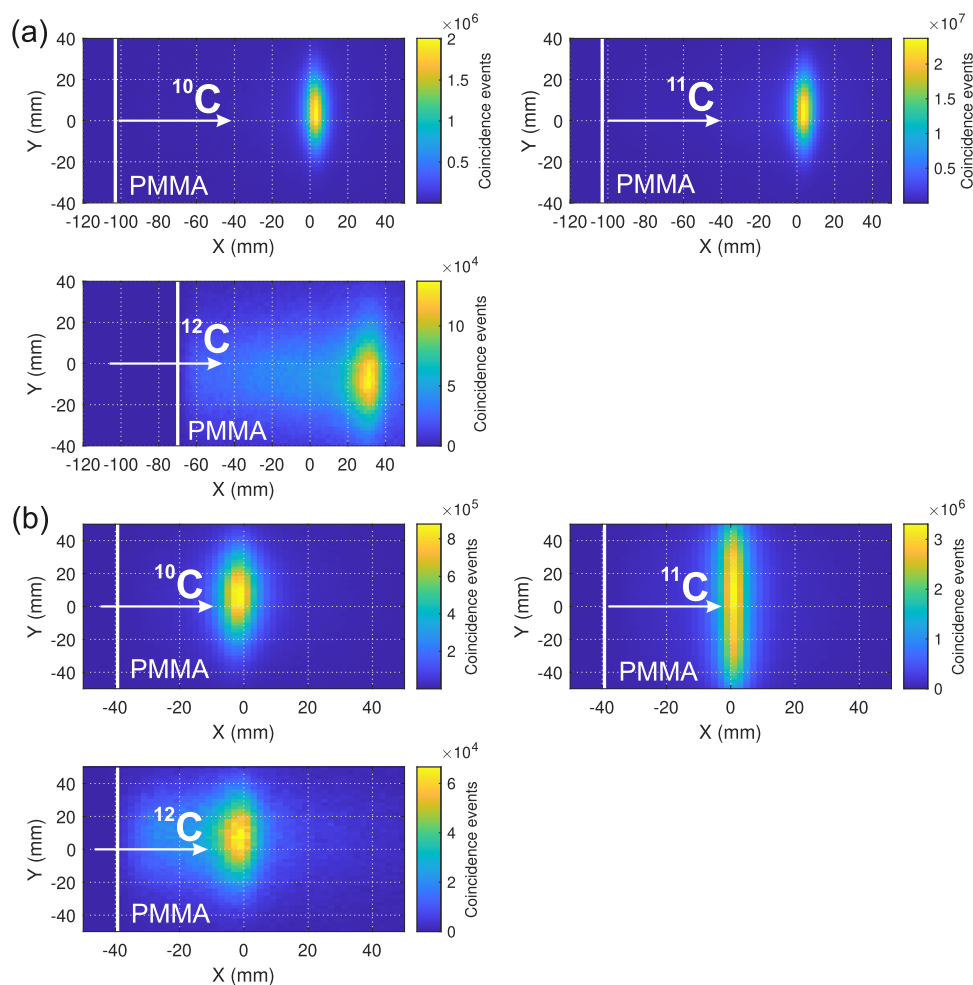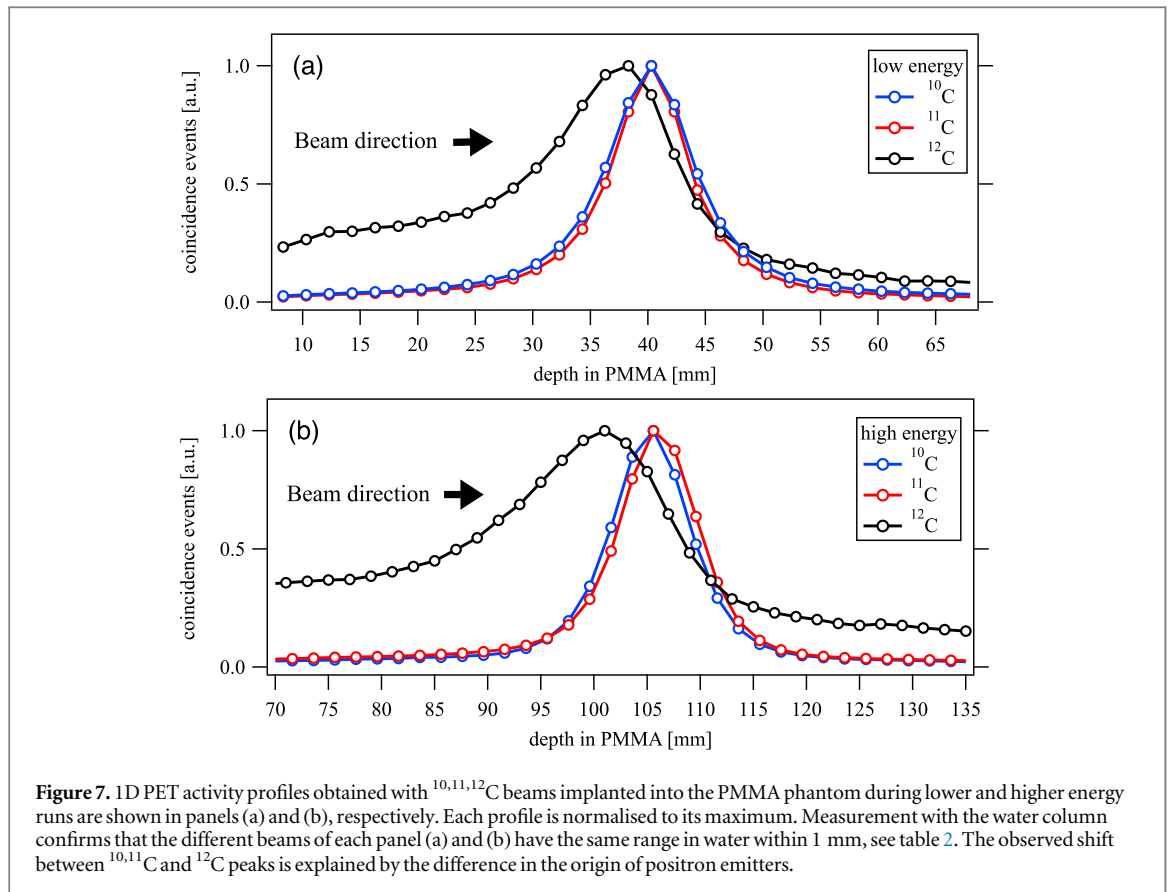
Figure 6. PET images of ^{10,11,12}C isotopes implanted into the PMMA phantom during higher and lower energy runs are shown in panels (a) and (b), respectively. The images are corrected for the sensitivity of the PET scanner and attenuation in the phantom. The pixel size of the image reconstruction is 2×2 mm^2. The image of ^{11}C in panel (b) is obtained during the FRS operation in mono-energetic mode, the others in achromatic mode. The position of the entrance face of the phantom and the beam direction are indicated by a vertical white line and white arrow, respectively.

Table 2. Ranges expressed in water equivalent thickness measured with PET scanner (range is defined as the position of the activity peak) from this work and with water column setup (range is defined as 80% of the maximum dose at the distal fall-off) from (Boscolo *et al* 2022). The conversion of range from PMMA to water equivalent thickness is performed using ATIMA version 1.2 (Scheidenberger and Geissel 1998). The comparison for ^{12}C high energy case is not shown because the beam conditions were not the same for the two setups during this measurement. Statistical and systematical uncertainties are indicated in the parenthesis.

Ion	Range expressed in water equivalent thickness (mm)	
	PET scanner	Water column
^{10}C	46.230 ± 0.008(stat.) ± 1(syst.)	46 ± 1
^{11}C	45.762 ± 0.003(stat.) ± 1(syst.)	46 ± 1
^{12}C	42.950 ± 0.053(stat.) ± 1(syst.)	46 ± 1
^{10}C	120.177 ± 0.007(stat.) ± 1(syst.)	121 ± 1
^{11}C	121.036 ± 0.001(stat.) ± 1(syst.)	122 ± 1

irradiation with positron-emitters, the activity of the stopped projectiles ^{10}C and ^{11}C is much more intense than the activity from fragmentation products. In addition, one can notice that for the higher energy irradiation, panel (b) of figure 7, the activity peaks are wider than in the lower energy case from panel (a). This effect is due to

Figure 7. 1D PET activity profiles obtained with ^{10,11,12}C beams implanted into the PMMA phantom during lower and higher energy runs are shown in panels (a) and (b), respectively. Each profile is normalised to its maximum. Measurement with the water column confirms that the different beams of each panel (a) and (b) have the same range in water within 1 mm, see table 2. The observed shift between ^{10,11}C and ^{12}C peaks is explained by the difference in the origin of positron emitters.
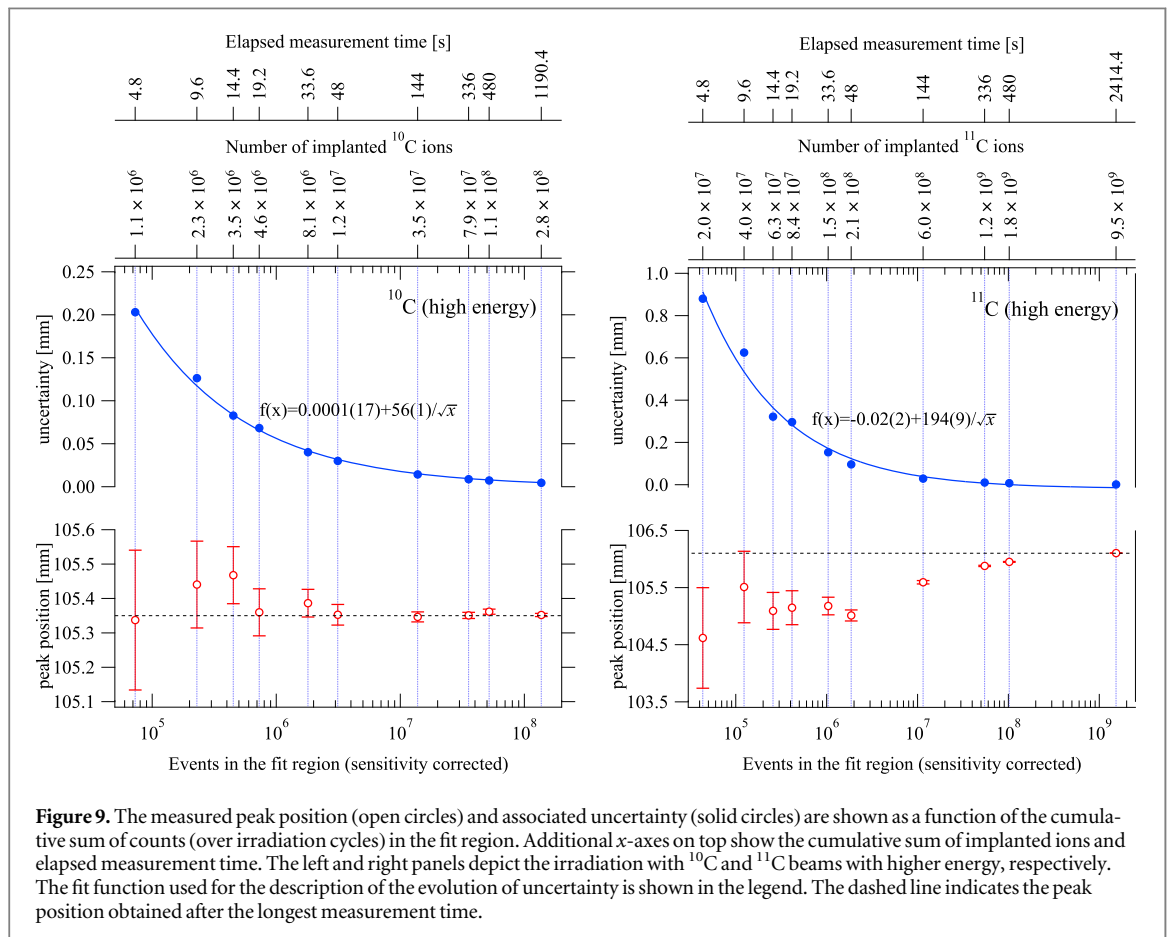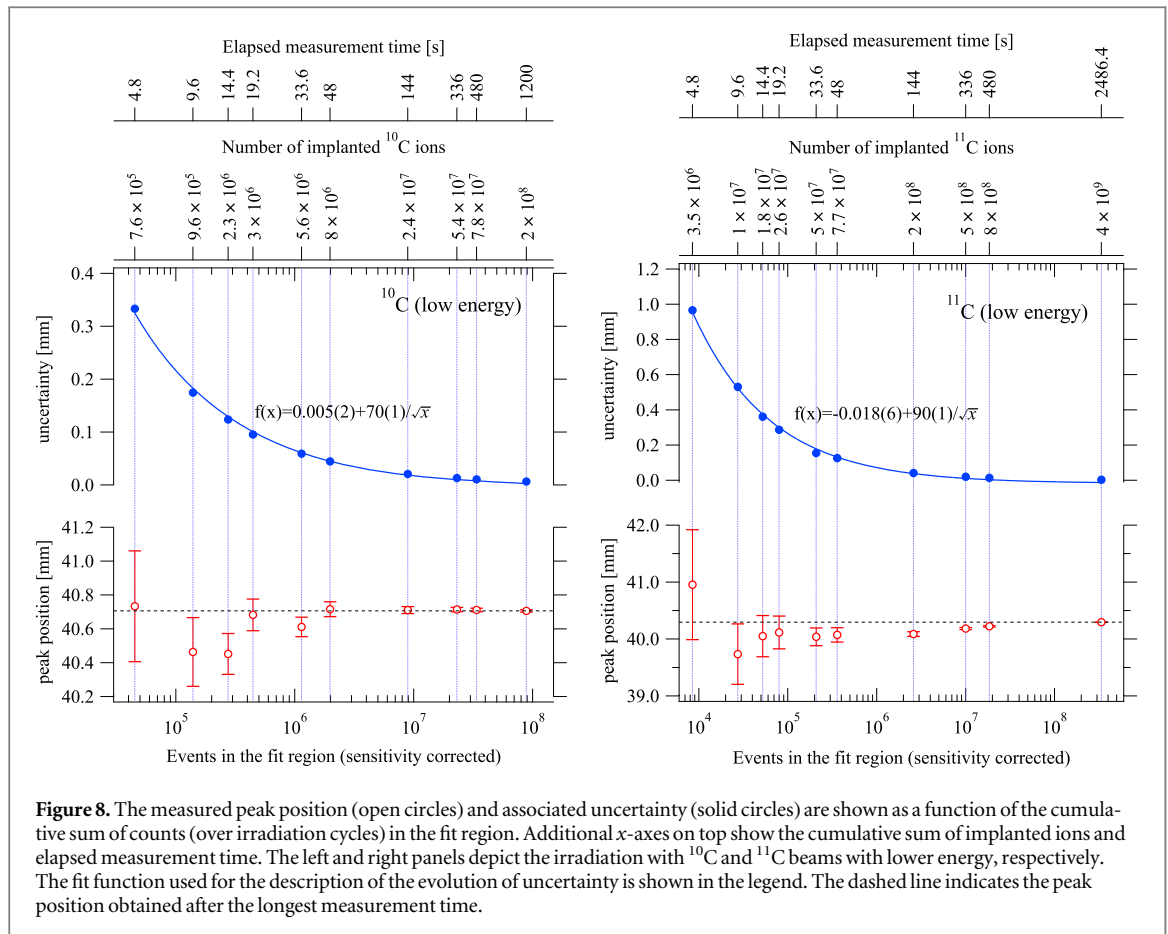
larger range straggling in the PMMA, considering that the energy spread of the beams at the entrance of the phantom was the same within 1%. The latter was independently measured by the standard beam identification detectors of FRS, see section 2.1.

3.3. Precision of PET activity range determination

The presented high-statistics data obtained with a commercial widely-used PET scanner allow us to study the precision of range determination as a function of the accumulated PET counts. The precision of range determination is quantified as the standard deviation of the peak position parameter of the GE fitting function, as described in section 2.3.5. The measured peak position and its uncertainty versus the cumulative number of PET counts in the fit region for the irradiation with ^{10,11}C beams of lower and higher energies are shown in figures 8 and 9, respectively. For a comprehensive description, the range is plotted versus two additional axes: the number of implanted ions as determined from the IC measurement and the elapsed measurement time (i.e. the time since the start of the irradiation).

For each measurement, the most precise peak position value is the one obtained with the highest statistics and we also consider this one to be the most accurate value here; it is thus the reference value for the data points with lower statistics. These reference values are indicated by the dashed lines in figures 8 and 9. For the lower energy ^{10}C irradiation, see figure 8 left panel, the first beam cycle of 4.8 s with 7.6×10^5 implanted ions already provides an accurate peak position value with a precision of 0.33 mm. The same conclusion holds for the ^{10}C irradiation of higher energy, see figure 9 left panel: an accurate peak position with a precision of 0.20 mm is reached with 1.1×10^6 ions after 4.8 s of irradiation.

In the case of the ^{11}C irradiation with lower energy, figure 8 right panel, the peak position also reaches an accurate value after 1 beam cycle, however with a three times larger uncertainty (0.97 mm) than in the ^{10}C low energy case. The peak position value in the higher energy run of ^{11}C, see figure 9 right panel, exhibits a growing behavior with increasing statistics. Fluctuations in the time structure of the spills were observed during parts of this irradiation. The corresponding data taken by the IC show up to 50% intensity fluctuations. This points toward the issues connected to the conditions of the primary beam. These disturbances were directly correlated in time with the beam sharing with another experimental area. These issues are under investigation. However, the above-described problem does not influence the determination of the peak position's uncertainty as an inverse square root behaviour is observed.

Figure 8. The measured peak position (open circles) and associated uncertainty (solid circles) are shown as a function of the cumulative sum of counts (over irradiation cycles) in the fit region. Additional *x*-axes on top show the cumulative sum of implanted ions and elapsed measurement time. The left and right panels depict the irradiation with ^{10}C and ^{11}C beams with lower energy, respectively. The fit function used for the description of the evolution of uncertainty is shown in the legend. The dashed line indicates the peak position obtained after the longest measurement time.

Figure 9. The measured peak position (open circles) and associated uncertainty (solid circles) are shown as a function of the cumulative sum of counts (over irradiation cycles) in the fit region. Additional *x*-axes on top show the cumulative sum of implanted ions and elapsed measurement time. The left and right panels depict the irradiation with ^{10}C and ^{11}C beams with higher energy, respectively. The fit function used for the description of the evolution of uncertainty is shown in the legend. The dashed line indicates the peak position obtained after the longest measurement time.

As anticipated, the uncertainty value decreases with the number of accumulated counts. In all considered cases, the uncertainty shows an inverse square root dependence on the number of events in the fit region, as expected for a purely statistical dependence. The corresponding fit parameters are indicated in the legends of figures 8 and 9. It should be noted that since the sensitivity/attenuation correction does not change much over the fitted region, the sensitivity-corrected data, which are used in the uncertainty analysis, preserve the counting statistics nature (Poisson statistics) of the raw, non-corrected, data. This behavior indicates that the non-statistical contributions to the precision are negligible.

4. Discussion

In this work, we study the precision with which the PET activity range can be determined using in-beam PET images of ^{10,11}C radioactive beams in homogeneous PMMA phantoms. For reference purposes, we also consider the PET images taken with a ^{12}C beam. The PET scanner used consists of two 225×220 mm^2 panels placed 35 cm apart. Each panel is a 4×4 array of Siemens Biograph mCT block detectors. We consider a situation in which the PET activity range is determined and/or updated in quasi-real time, at the time scale of a few seconds, the typical period of the time structure of synchrotron spills. In this context, one needs a quick image reconstruction method. We create 2D images as the 2D histograms of the crossing points of the LORs with the central plane of the beam (in our case the mid-plane between the scanner panels). The 1D positron activity profiles derived from the 2D images are fitted using the GE function, with the uncertainty of the PET activity range defined as the uncertainty on the fit parameter which represents the position of the maximum activity. We investigated the time evolution of the PET activity range uncertainty and precision during the course of irradiation, and show that the uncertainty improves with the inverse square root of the number of PET counts. The uncertainty is thus fully determined by the PET counting statistics. Our results can be used to estimate the contribution of PET counting statistics to the precision of range determination in a particular carbon therapy situation.

As an example, assume a typical clinical ^{12}C irradiation in which a dose of 2 Gy (RBE) is deposited in a water volume of $100 \times 100 \times 100$ mm^3 located at 150 mm depth. This irradiation requires a total of 2.8×10^9 ^{12}C ions in 34 energy slices spaced 3 mm apart. The highest-weighted slice comprises 4×10^8 ions. If we scale the latter number to a 10×10 mm^2 lateral area, the required number of ions becomes 4×10^6. We assume here the same RBE for all studied isotopes of carbon, such that the same number of ions is required for the same dose. In our experiments, the ^{10}C beam intensity was about 10 times smaller than the ^{11}C intensity for the low-energy beams, and about 20 times smaller for the high-energy beams. Let us first consider a situation in which 4×10^6 ions are delivered in 1 spill and the PET activity range is determined from the data measured during that spill. For the high energy beams, see figure 9, we deduce a PET activity range uncertainty of 0.10 mm for ^{10}C and 2.0 mm for ^{11}C after delivery of 4×10^6 ions in the first 4.8 s spill. This large difference results from the much faster decay of ^{10}C (the half-life is 64 times smaller) and the fact that, contrary to ^{11}C, the beam-on data are included. A comparison with the results for the stable isotope ^{12}C beam can not be made because insufficient PET counts are collected during the first spill. We needed at least 4 spills of ^{12}C to collect sufficient PET counts, see figure 10. Let us therefore compare the situation after 4 spills, a measurement time of 19.2 s, and 4 times $4 \times 10^6 = 1.6 \times 10^7$ ions. The PET activity range uncertainty for ^{10}C, ^{11}C and ^{12}C is 0.04 mm, 0.7 mm and 1.3 mm, respectively. The gain in accuracy related to the PET counting statistics is thus much larger when going from ^{11}C to ^{10}C than when going from ^{12}C to ^{11}C.

It should be noted that the peak position of ^{12}C shifts towards larger depths in PMMA as the irradiation progresses. We verified that this is not due to the unstable behaviour of the primary beam from the accelerator. The trend can be explained as follows. The production of ^{11}C fragments in the PMMA phantom is an order of magnitude higher than that of ^{10}C fragments (Horst *et al* 2019), and the peak of stopped ^{11}C fragments is about 2 mm deeper than that of ^{10}C fragments. The measured activity is dominated by the decay of ^{10}C during the first few minutes of the irradiation, and increasingly dominated by the decay of ^{11}C after that. Thus, the position of the activity peak is expected to increase with the irradiation time by about 2 mm during the 1017.6 s of irradiation.

The uncertainty and accuracy of determining the dose range from the PET activity range includes factors other than the PET count statistics, which is the focus of this work. For stable beams, there is a shift between the dose range and the PET activity range, whose magnitude is proportional to the implantation depth (Fiedler *et al* 2012). In our case, this shift is 3 mm for ^{12}C, and for ^{10,11}C there is no difference within the systematic errors, see table 2. See also similar studies by (Mohammadi *et al* 2019, Chacon *et al* 2020). Considering patient treatment, the accuracy of PET scanner positioning relative to the patient and the beam isocenter will play a role as well. The results presented here make us conclude that the statistical contribution to the uncertainty of a dose range measurement will be negligible for irradiation with ^{10}C ions from the very start of the irradiation, i.e. already after a

Figure 10. The measured peak position (open circles) and associated uncertainty (closed circles) are shown as a function of the cumulative sum of counts (over irradiation cycles) in the fit region. Additional *x*-axes on top show the cumulative sum of implanted ions and elapsed measurement time. The irradiation with ^{12}C beam with lower energy is shown. The fit function used for the description of the evolution of uncertainty is shown in the legend. The dashed line indicates the peak position obtained after the longest measurement time.

few seconds (1 beam spill). During irradiation with ^{11}C ions, it will take a longer time before the statistical contribution becomes negligible.

The dependence of the range uncertainty on the number of implanted ^{10}C ions is discussed also in the work (Iseki *et al* 2004). Iseki *et al* (2004) take the peak position resulting from a fit of the activity distribution with a Gaussian function as the activity range, and determine a range uncertainty of ± 0.3 mm for irradiation with around 3×10^{5} particles. We have shown that the GE function provides a better description of the activity peak since it takes the tails of the distribution into account, see figure 4. The PET activity range uncertainty is similar to the value we obtained for the same number of implanted ^{10}C ions. Given that PET scanners with similar efficiency were used, our work and the work of Iseki *et al* (2004) are in agreement.

The image reconstruction algorithm used in this work is a 2D reconstruction approach in which events can be simply added to an image as they are collected during irradiation. The computational burden is very low. For example, the typical time required to obtain an ion beam image using 10^{6} events during the present analysis is below 0.5 s using MATLAB software. The highest event rate measured in our work, at the end of the irradiation with the ^{10}C ions, is close to 10^{4} events per second, much lower than typically present in a PET scan in nuclear medicine. The relatively low event rate and simple image reconstruction algorithm, combined with modern computational infrastructure will allow quasi-real-time 2D feedback during irradiations with radioactive ion beams.

5. Conclusions

We show that the uncertainty in determining the PET activity peak resulting from the implantation of ^{10,11,12}C in PMMA is fully determined by counting statistics: it scales inversely with the square root of the number of PET counts, and the systematic uncertainty (i.e. the asymptotic value for a very large number of PET counts) is very small (less than 0.02 mm). Because of the much shorter half-life of ^{10}C relative to ^{11}C, ^{10}C provides better range verification capabilities: the precise activity range is obtained much quicker (for a given number of implanted

ions) and in-spill events can be used because the beam-related prompt coincidence rate is small compared to the true positron annihilation coincidence rate. Furthermore, biological washout will be reduced significantly for ^{10}C compared to ^{11}C due to the shorter half-life. These advantages make the ^{10}C beam attractive for range measurements during ion beam radiotherapy, provided high enough beam intensities are available. The numerical results presented in this paper can be used to estimate the impact of PET counting statistics on the precision of range determination in a particular carbon therapy situation.

Acknowledgments

ORCID iDs

S Purushothaman ⓘ https://orcid.org/0000-0003-0526-4913
P Dendooven ⓘ https://orcid.org/0000-0003-1859-1315
E Haettner ⓘ https://orcid.org/0000-0002-5057-9853
D Boscolo ⓘ https://orcid.org/0000-0001-5709-4472
C Graeff ⓘ https://orcid.org/0000-0002-5296-7649
M Durante ⓘ https://orcid.org/0000-0002-4615-553X

References

Angert N and Schmelzer C 1969 The UNILAC, a variable energy linear accelerator for atomic ions of any mass *Kerntech* **11** 690–5
Bé M-M *et al* 2010 *Table of radionuclides (Vol. 5 - A = 22 to 244), Vol. 5 of Table of radionuclides* (Bureau International des Poids et Mesures)
Boscolo D (the Super-FRS Experiment Collaboration) *et al* 2021 Radioactive beams for image-guided particle therapy: the BARB experiment at GSI *Frontiers Oncol.* **11** 737050
Boscolo D *et al* 2022 Depth dose measurements in water for ^{11}C and ^{10}C beams with therapy relevant energies *Nucl. Instrum. Methods Phys. Res. Sect. A* **1043** 167464
Castro J R, Quivey J M, Lyman J T, Chen G T Y, Phillips T L, Tobias C A and Alpen E L 1980 Current status of clinical particle radiotherapy at lawrence berkeley laboratory *Cancer* **46** 633–41
Chacon A *et al* 2020 Experimental investigation of the characteristics of radioactive beams for heavy ion therapy *Med. Phys.* **47** 3123–32
Chatterjee A, Alpen E L, Tobias C A, Llacer J and Alonso J 1981 High energy beams of radioactive nuclei and their biomedical applications *Int. J. Radiat. Oncol.* *Biol.* *Phys.* **7** 503–7
Chatterjee A, Saunders W, Alpen E, Alonso J, Scherer J and Llacer J 1982 Physical measurements with high-energy radioactive beams *Radiat. Res.* **92** 230–44
Durante M, Debus J and Loeffler J S 2021 Physics and biomedical challenges of cancer therapy with accelerated heavy ions *Nat. Rev. Phys.* **3** 777–90
Durante M and Parodi K 2020 Radioactive beams in particle therapy: past, present, and future *Frontiers .Phys.* **8** 1–13
Enghardt W, Crespo P, Fiedler F, Hinz R, Parodi K, Pawelke J and Poenisch F 2004 Charged hadron tumour therapy monitoring by means of PET *Nucl. Instrum. Methods Phys. Res. A* **525** 284–8
Enghardt W, Debus J, Haberer T, Hasch B, Hinz R, Jäkel O, Krämer M, Lauckner K, Pawelke J and Pönisch F 1999 Positron emission tomography for quality assurance of cancer therapy with light ion beams *Nucl. Phys. A* **654** 1047c–1050c
Enghardt W, Fromm W, Manfrass P and Schardt D 1992 Limited-angle 3D reconstruction of PET images for dose localization in light ion tumour therapy *Phys. Med. Biol.* **37** 791
Fiedler F, Kunath D, Priegnitz M and Enghardt W 2012 *Online Irradiation Control by Means of PET, in 'Ion Beam Therapy'* (Berlin: Springer) 527–43
Fiedler F, Shakirin G, Skowron J, Braess H, Crespo P, Kunath D, Pawelke J, Pönisch F and Enghardt W 2010 On the effectiveness of ion range determination from in-beam PET data *Phys. Med. Biol.* **55** 1989
Geissel H, Schwab T, Armbruster P, Dufour J, Hanelt E, Schmidt K-H, Sherrill B and Münzenberg G 1989 Ions penetrating through ion-optical systems and matternon-liouvillian phase-space modelling *Nucl. Instrum. Methods Phys. Res. A* **282** 247–60
Geissel H *et al* 1992 The GSI projectile fragment separator (FRS): a versatile magnetic system for relativistic heavy ions *Nucl. Instrum. Methods Phys. Res. B* **70** 286–97
Horst F *et al* 2019 Measurement of PET isotope production cross sections for protons and carbon ions on carbon and oxygen targets for applications in particle therapy range verification *Phys. Med. Biol.* **64** 205012
Iseki Y, Kanai T, Kanazawa M, Kitagawa A, Mizuno H, Tomitani T, Suda M and Urakabe E 2004 Range verification system using positron emitting beams for heavy-ion radiotherapy *Phys. Med. Biol.* **49** 3179
Jakoby B W, Bercier Y, Conti M, Casey M E, Bendriem B and Townsend D W 2011 Physical and clinical performance of the mCT time-of-flight PET/CT scanner *Phys. Med. Biol.* **56** 2375–89

Janik R *et al* 2011 Time projection chambers with C-pads for heavy ion tracking *Nucl. Instrum. Methods. Phys. Res.* A **640** 54–7

Kanazawa M *et al* 2002 Application of an RI-beam for cancer therapy: *in-vivo* verification of the ion-beam range by means of positron imaging *Nucl. Phys.* A **701** 244–52

Knopf A-C and Lomax A 2013 In vivo proton range verification: a review *Phys. Med. Biol.* **58** R131–60

Kraan A C 2015 Range verification methods in particle therapy: underlying physics and Monte Carlo modeling *Frontiers Oncol.* **5** 150

Kurcewicz J *et al* 2012 Discovery and cross-section measurement of neutron-rich isotopes in the element range from neodymium to platinum with the FRS *Phys. Lett.* B **717** 371–5

Liu W, Zhang X, Li Y and Mohan R 2012 Robust optimization of intensity modulated proton therapy *Med. Phys.* **39** 1079–91

Llacer J, Chatterjee A, Alpen E, Saunders W, Andreae S and Jackson H 1984 Imaging by injection of accelerated radioactive particle beams *IEEE Trans. Med. Imaging* **3** 80–90

Llacer J, Chatterjee A, Jackson H C, Lin J C and Zunzunegui M V 1979 An imaging instrument for positron emitting heavy ion beam injection *IEEE Trans. Nucl. Sci.* **26** 634–47

Maccabee H D, Madhvanath U and Raju M R 1969 Tissue activation studies with alpha-particle beams *Phys. Med. Biol.y* **14** 213

Mohammadi A, Tashima H, Iwao Y, Takyu S, Akamatsu G, Nishikido F, Yoshida E, Kitagawa A, Parodi K and Yamaya T 2019 Range verification of radioactive ion beams of ^{11}C and ^{15}O using in-beam PET imaging *Phys. Med. Biol.* **64** 145014

Ozoemelam I, van der Graaf E, van Goethem M-J, Kapusta M, Zhang N, Brandenburg S and Dendooven P 2020a Feasibility of quasi-prompt PET-based range verification in proton therapy *Phys. Med. Biol.* **65** 245013

Ozoemelam I, van Der Graaf E, van Goethem M-J, Kapusta M, Zhang N, Brandenburg S and Dendooven P 2020b Real-time PET imaging for range verification of helium radiotherapy *Front. Phys.* **8** 565422

Parodi K 2015 Vision 20/20: positron emission tomography in radiation therapy planning, delivery, and monitoring *Med. Phys.* **42** 7153–68

Parodi K, Enghardt W and Haberer T 2002 In-beam PET measurements of β^+ radioactivity induced by proton beams *Phys. Med. Biol.* **47** 21–36

Pawelke J, Enghardt W, Haberer T, Hasch B, Hinz R, Kramer M, Lauckner E and Sobiella M 1997 In-beam PET imaging for the control of heavy-ion tumour therapy *IEEE Trans. Nucl. Sci.* **44** 1492–8

Pflugfelder D, Wilkens J J and Oelfke U 2008 Worst case optimization: a method to account for uncertainties in the optimization of intensity modulated proton therapy *Phys. Med. Biol.* **53** 1689–700

Routti J and Prussin S 1969 Photopeak method for the computer analysis of gamma-ray spectra from semiconductor detectors *Nucl. Instrum. Methods* **72** 125–42

Scheidenberger C and Geissel H 1998 Penetration of relativistic heavy ions through matter *Nucl. Instrum. Methods Phys. Res.* B **135** 25–34

Scheidenberger C *et al* 2003 Energy and range focusing of in-flight separated exotic nuclei—a study for the energy-buncher stage of the low-energy branch of the Super-FRS *Nucl. Instrum. Methods Phys. Res.* B **204** 119–23 14th International Conference on Electromagnetic Isotope Separators and Techniques Related to their Applications

Smeets J *et al* 2012 Prompt gamma imaging with a slit camera for real-time range control in proton therapy *Phys. Med. Biol.* **57** 3371–405

Steiner M, Blasche K, Clerc H-G, Eickhoff H, Franczak B, Geissel H, Münzenberg G, Schmidt K-H, Stelzer H and Sümmerer K 1992 Preliminary measurements of SIS-18 beam parameters *Nucl. Instrum. Methods Phys. Res. Sect.* A **312** 420–4

Stelzer H and Voss B 2002 Ionization chamber for ion beams and method for monitoring the intensity of an ion beam U.S. Patent No. 6,437,513

Stolz A *et al* 2002 Projectile fragmentation of ^{112}Sn at $E_{lab} = 1 AGeV$ *Phys. Rev.* C **65** 064603

Tarasov O and Bazin D 2008 LISE++: radioactive beam production with in-flight separators *Nucl. Instrum. Methods Phys. Res.* B **266** 4657–64 Proceedings of the XVth International Conference on Electromagnetic Isotope Separators and Techniques Related to their Applications

Tobias C A, Lawrence J H, Born J L, McCombs R K, Roberts J E, Anger H O, Low-Beer B V A and Huggins C B 1958 Pituitary irradiation with high-energy proton beams a preliminary report *Cancer Res.* **18** 121–34

Toramatsu C *et al* 2018 Washout effect in rabbit brain: in-beam PET measurements using ^{10}C, ^{11}C and ^{15}O ion beams *Biomed. Phys. Eng. Express* **4** 035001

Unkelbach J, Chan T C Y and Bortfeld T 2007 Accounting for range uncertainties in the optimization of intensity modulated proton therapy *Phys. Med. Biol.* **52** 2755–73

Weick H *et al* 2000 Slowing down of relativistic few-electron heavy ions *Nucl. Instrum. Methods Phys. Res.* B **164–165** 168–79

Wolf M, Anderle K, Durante M and Graeff C 2020 Robust treatment planning with 4D intensity modulated carbon ion therapy for multiple targets in stage IV non-small cell lung cancer *Phys. Med. Biol.* **65** 215012